Temperature-Dependent Multi-Scale Pore Evolution and Nitrogen Diffusion in Nuclear Graphite

LONGKUI ZHU, MENGHE TU, ZHENGCAO LI, MINGYANG LI, WEI MIAO, HONG LI, and ALEX A. VOLINSKY

Two- and three-dimensional pore evolutions along with nitrogen diffusion behavior in nuclear graphite were studied using thermogravimetric analysis, X-ray computed tomography, scanning electron microscopy, and the Brunauer-Emmett-Teller method. Calculated nitrogen diffusion activation energy was approximately 2.5 kJ·mol^{-1}. Stable weight loss of graphite specimens increased with temperature, primarily due to more escaped nitrogen from the graphite matrix. Fewer nano-pores and more micro-pores were formed because of the nano-pore coalescence. At 873 K (600 °C), graphite microstructure evolution might be induced by temperature and mild oxidation. Before being placed into high temperature gas-cooled reactors (HTGRs), porous nuclear graphite should be subjected to vacuum at 573 K to 673 K (300 °C to 400 °C) to minimize ^{14}N in the pores and ^{14}C generated during operation of HTGRs.

DOI: 10.1007/s11661-017-4076-z
© The Minerals, Metals & Materials Society and ASM International 2017

I. INTRODUCTION

NUCLEAR graphite is used extensively for moderators, reflectors, and structural materials in high-temperature gas-cooled reactors (HTGRs) because of its excellent irradiation performance and adequate mechanical properties at high temperatures.[1,2] There are both nano- (2 to 500 nm) and micro- (>500 nm) pores in nuclear graphite, hence nitrogen at approximately 1 bar pressure is inevitably present in the porous structures due to processing, transporting, and storing nuclear graphite.[3–6] During HTGRs operation, ^{14}C radiocarbons are produced by the reactions of ^{14}N isotope and thermal neutrons, further leading to ^{14}C release from nuclear graphite.[7] It is deduced that graphite microstructure and gas diffusion behavior have crucial effects on minimizing radiocarbons.

In HTGRs, porous nuclear graphite is exposed to high temperatures, neutron irradiation, oxidation, and other deleterious environments. Among these, much effort was devoted to studying synergistic effects of temperature and other factors on graphite microstructure. Huang *et al.*[8,9] investigated nuclear graphite oxidation in air at temperatures ranging from 973 K (700 °C) to 1373 K (1100 °C), and correlated oxidation behavior with the theory of active sites in graphite. Different oxidation mechanisms were proposed in terms of various reaction temperatures.[7,9–15] It is considered that open pores were first oxidized up to about 873 K (600 °C), while the strength gradually decreased with weight loss. When the reaction temperature was close to 1123 K (850 °C), the oxidation rate became slower in open pores due to the restricted oxygen diffusion rate. Then oxidation reactions ceased in open pores, and just the external graphite surfaces were oxidized above approximately 1123 K (850 °C). In these processes, multi-scale graphite pores with different morphology were formed at low and high temperatures. Wang *et al.*[16] believe that the micro-pores nucleated and grew during low-temperature oxidation, but the ligaments between the sub-micron pores collapsed and these pores coalesced to form larger pores at high temperatures. Chen *et al.*[3] think that the micro-pore size became increasingly larger with oxidation of IG-110 and HSM-SC nuclear graphite at 873 K (600 °C) or 1073 K (800 °C). Surface pore structure obviously changed when more weight of oxidized graphite was lost in the 14 pct CO_2 atmosphere at 1418 K (1145 °C). In summary, the above observations showed that graphite microstructure could evolve in terms of different oxidation mechanisms at various temperatures, which acted as the key factor for controlling microstructure evolution at the micron scale.

Similarly, it was also investigated how temperature and neutron irradiation synergistically affected graphite microstructure evolution. At room temperature, there are tetrahedral and octahedral interstices, along with a_0 = 0.246 nm and c_0 = 0.671 nm lattice parameters in A3-3 nuclear graphite. Under irradiation, graphite single crystals were usually subjected to lattice expansion in the *c* direction or shrinkage perpendicular

LONGKUI ZHU, ZHENGCAO LI, MINGYANG LI, and WEI MIAO are with the State Key Laboratory of New Ceramics & Fine Processing, Key Laboratory for Advanced Materials of Ministry of Education, School of Materials Science and Engineering, Tsinghua University, Beijing 100084, P.R. China. Contact e-mail: zcli@tsinghua.edu.cn MENGHE TU is with the Department of Reactor Engineering Research and Design, China Institute of Atomic Energy, Beijing 102413, P.R. China. HONG LI is with the Institute of Nuclear and New Energy Technology, Tsinghua University, Beijing 100084, P.R. China. ALEX A. VOLINSKY is with the Department of Mechanical Engineering, University of South Florida, Tampa, FL 33620. Contact e-mail: volinsky@usf.edu
Manuscript submitted June 14, 2016.
Article published online March 24, 2017

to basal planes.[17,18] As obtained both experimentally and numerically, thermal expansion in the *c* direction is substantially larger than in the *a* direction,[19,20] and graphite samples tended to be constrained during cooling.[17] Chang and Tsai *et al.*[21,22] found that the d-spacing of {0002} planes expanded from 0.336 nm to 0.396 nm and the *c* lattice parameter increased by approximately 18 pct due to the formation of numerous Frenkel pairs within the graphite sample irradiated with 10 dpa at 873 K (600 °C). Campbell *et al.*[23–25] demonstrated that the *c* spacing increase and crystallite dimensions decrease with temperature in fine-grain nuclear graphite resulted from higher dose rates, while the plateau value of the mean coefficient of thermal expansion was similar for all irradiation temperatures. Krishna *et al.*[26] discovered that the average crystalline size of graphite decreased with the received dose ranging from 0.1 dpa to 1.45 dpa at low temperatures [<523 K (250 °C)]. Recent research shows that microstructure did not display any observable changes at low doses and temperatures, while closing of pre-existing Mrozowski cracks was detected in IG-110 graphite samples irradiated to 6.7 dpa at 967 K (694 °C).[27] *In situ* observations using transmission electron microscopy show that the Mrozowski nano-cracks also closed at elevated temperatures.[28] Although lots of experiments were carried out, it is still unknown whether the significant structural evolution within nuclear graphite originated from neutron irradiation or temperature. Further experimental research is necessary to study how high temperature affected nuclear graphite microstructure evolution mechanisms.

A series of novel measurement techniques, including synchrotron X-ray computed tomography (XCT) and neutron diffraction, were employed to characterize three-dimensional and nano-scale defects of porous or cracked structures.[29–35] Marrow and Mostafavi *et al.*[29–33] systematically investigated elastic behavior and fracture by analyzing bulk elastic modulus, crack geometry and crack opening displacement in quasi-brittle graphite. The existence of the cohesive fracture process zone ahead of the crack tip was demonstrated at the micron scale. Likewise, it is feasible to identify temperature effects on graphite microstructure evolution by XCT. This work aims to investigate two- and three-dimensional pore structure and distribution along with graphite weight change in the processes of nitrogen diffusion from atmosphere to vacuum at different temperatures using XCT, scanning electron microscopy (SEM), and so on. Multi-scale pore evolution mechanisms are discussed in detail and key temperature parameters are determined to make sure that less nitrogen was present in HTGRs.

II. EXPERIMENTAL PROCEDURE

The 6 mm diameter spherical specimens were made from A3-3 porous nuclear graphite produced by Toyo Tanso Co., Ltd in Japan. Its as-received mechanical properties measured by the manufacturer at slow strain rate tensile and three-point bending tests are as follows. Dynamic elastic modulus: 10.2 GPa; bending strength: 37.2 MPa; compression strength: 76.8 MPa; fracture strength: 25.3 MPa. The specimens were placed into a high temperature resistant ceramic container of the Rubotherm thermogravimetric analyzer (TGA), which had 10 μg weight resolution. At each temperature, a contrast TGA experiment without any graphite specimen was performed to minimize temperature, pressure, and gas flow effects on graphite weight change. Then TGA experiments with the specimens were carried out using the same parameters and repeated three times. Weight change of each specimen was obtained by subtracting the data obtained with and without the specimen. The whole TGA experiment was composed of the four stages, including pre-vacuum treatment with the vacuum pressure of approximately 4×10^{-7} bar, nitrogen injection, nitrogen diffusion, and system recovery. The first stage of the pre-vacuum treatment is to remove oxygen, moisture, and other impurity gases inside the open pores. Then 99.999 pct pure nitrogen was injected into the specimens in vacuum with the flow of 50 standard cubic centimeters per minute (sccm). Gases consisted of ≤3 ppm O_2, ≤1 ppm H_2, ≤3 ppm ΣC (CO and CO_2), and ≤6 ppm H_2O apart from nitrogen. In the third stage of nitrogen diffusion, it took less than 5 min to reach 4×10^{-7} bar vacuum from 1 bar at every temperature, and real-time weight changes of the specimens were recorded when the system was subjected to vacuum and constant temperature. At the final stage, nitrogen-diffused specimens were cooled by 50 sccm room temperature helium with recovery of the TGI system. Table I gives key parameters of each stage. Afterwards, typical morphology of the specimen surfaces was characterized by SEM. The Brunauer-Emmett-Teller (BET) and Archimede's weight-volume methods were employed to calculate nano-pore volume and total porosity of the graphite specimens, respectively. The classical BET principle is the multi-layer nitrogen molecular adsorption and desorption on nano-pore surfaces based on the hypothesis of surface homogeneity and self-adsorption of nitrogen molecules. Since the nano-pores might not be filled with nitrogen molecules, there were some errors in characterizing the nano-pore volume. In our experiments, relative nano-pore volume at different temperatures was calculated using the same BET method. Before the measurement of the total porosity by the Archimede's weight-volume method, the apparent density was first calculated in terms of the mass and volume of each graphite specimen using the ML204 electronic balance and the micrometer three times, and the true density was measured by mercury porosimetry.

In addition, roughly 1 mm diameter cylindrical samples for XCT were prepared by wire electrode cutting. Prior to experiments using the BL13W1 beam line at the Shanghai Synchrotron Radiation Facility (SSRF), the samples were degreased with acetone in an ultrasonic cleaner, washed with deionized water, dried by hot air, and used to examine two- and three-dimensional morphology of virgin graphite samples. In order to perform tomographic imaging, almost monochromatic X-ray beam was utilized with the energy of 14 keV, and a

Table I. Key Parameters of Each Experimental Stage Using the Themogravimetric Instrument with Magnetic Suspension Balance

Experimental Stages	Pressure (Bar)	Temperature [K (°C)]	Temperature Ramping Rate [K (°C)·min^{-1}]	Time (min)	Gas Flow (sccm)
Pre-vacuum treatment	0	293 (20) or 473 (200)	20	30	0
Nitrogen injection	1	293 (20), 473 (200), 673 (400), 873 (600) or 1073 (800)	10	60–120	50
Nitrogen diffusion	0	293 (20), 473 (200), 673 (400), 873 (600) or 1073 (800)	0	120	0
System recovery	1	293 (20)	20	30	0

high-speed camera 0.1 m away from a virgin sample recorded transmitted intensity in a 5 seconds exposure/projection interval, while the sample was rotated in 0.2 deg increments. During each 180 deg rotation, 900 two-dimensional radiographs were saved and applied for reconstruction of image slices. Isotropic voxels with the resolution of 0.7 μm were achieved in the reconstructed slices. Next, image analysis, visualization, and three-dimensional rendering were carried out using Amira commercial software package.[35] The exterior-inside threshold value of image gray scale ranging from 0 to 255 was defined as 55 to calculate the volume of the pores and the graphite matrix. For the XCT-tested sample, the real-time weight change experiments by TGA were first carried out during the nitrogen diffusion process at 1073 K (800 °C). Second, three-dimensional morphology at local zones was also reconstructed using XCT, the Amira software, and the same experimental parameters to further clarify the high-temperature evolution mechanisms in graphite microstructure.

III. RESULTS AND DISCUSSION

A. *Weight Change and Diffusion Activation Energy*

Real-time weight of spherical graphite specimens at different temperatures is illustrated in Figure 1. Obvious weight change took place during nitrogen diffusion processes when the systems were subjected to vacuum and constant temperatures. It took approximately 30 to 60 minutes to reach steady stage at every temperature. When maximum amount of nitrogen molecules diffused outside from the specimen matrix, dynamic balance of nitrogen diffusion was reached. As shown in Figure 1, each curve for weight *vs* time was fitted with the Boltzmann function, Eq. [1]. The Boltzmann function is:

$$y = \frac{A_1 - A_2}{1 + e^{(x - x_0)/dx}} + A_2, \qquad [1]$$

where x is time; y is the weight change of nuclear graphite; A_1 is approximately equal to the initial y value; A_2 is the y value at the steady stage. According to Eq. [1], the stable weight change at various temperatures was obtained, as shown in Figure 2. It is found that these values gradually decreased from room temperature to 673 K (400 °C). The minimum values, also named as the peak weight loss, simultaneously appeared at about 673 K and 1073 K (400 °C and 800 °C). That is, the least amount of nitrogen was left inside the graphite specimens. From the viewpoint of minimizing ^{14}N and ^{14}C, porous nuclear graphite should be first subjected to vacuum at 573 K to 673 K (300 °C to 400 °C) before being placed into reactors. Besides, stable weight loss became smaller at 873 K (600 °C) compared with 673 K and 1073 K (400 °C and 800 °C).

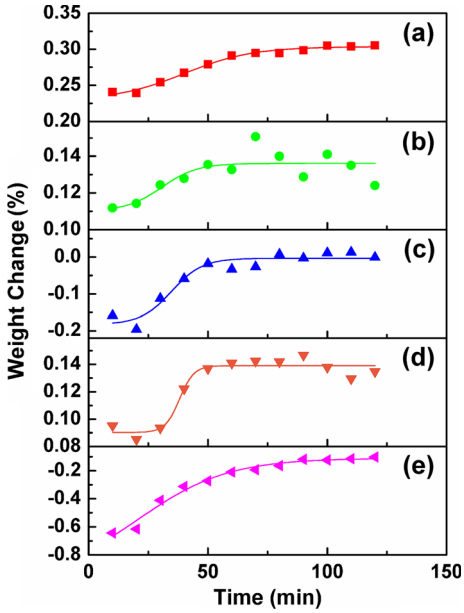

Fig. 1—Real-time weight change of graphite specimens during nitrogen diffusion at different temperatures: (*a*) Room temperature [approximately 293 K (20 °C)], (*b*) 473 K (200 °C), (*c*) 673 K (400 °C), (*d*) 873 K (600 °C), and (*e*) 1073 K (800 °C).

In essence, hexagonal graphite weight loss originated from the escape of nitrogen molecules from the graphite matrix. The largest diffusion distance was the core-to-surface radius, r, of the 6 mm diameter spherical specimen. Referring to the Fick's law and hydrogen diffusion in crystals,[36,37] the diffusion coefficient, D, is:

$$D = \frac{r^2}{6t_{0.95}}, \qquad [2]$$

where $t_{0.95}$ is time taken when the weight change is 0.95 of the stable value through the time-delay method.[37] Substituting $r \approx 3$ mm and values of $t_{0.95}$ given in Figure 1 into Eq. [2] yields the nitrogen diffusion coefficient, D, as an average for the three

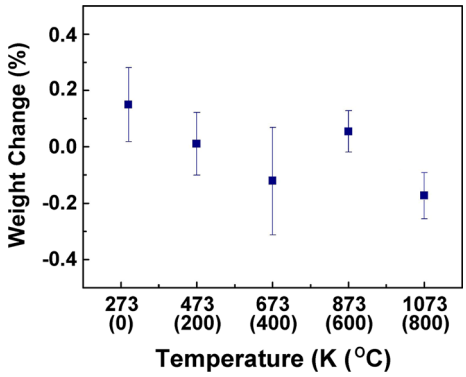

Fig. 2—Stable weight change of graphite specimens during nitrogen diffusion processes at different temperatures, where the minimum values, also named as the peak weight loss, simultaneously appeared at about 673 K and 1073 K (400 °C and 800 °C).

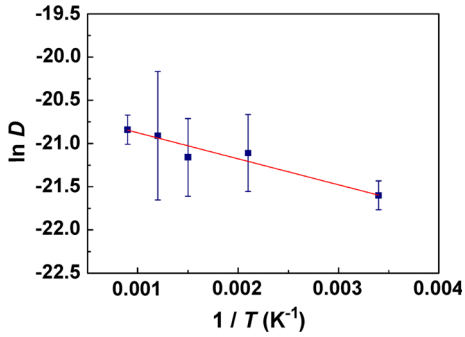

Fig. 3—Natural logarithms of D (the nitrogen diffusion coefficient), ln$D$, *vs* the reciprocal temperature, $1/T$, where the slope of the fitted line is −300.7.

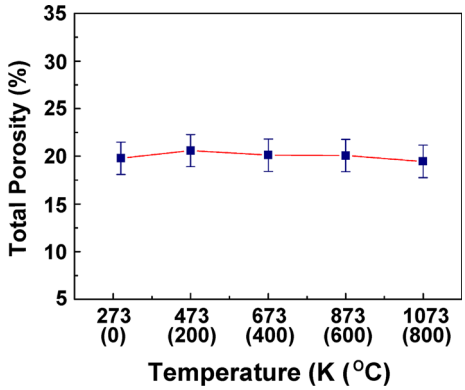

Fig. 4—Variation of the total porosity of nuclear graphite diffused with temperature, where the total porosity is about 20 pct at different temperatures.

experiments at 293 K (20 °C) of $(4.17 \pm 0.03) \times 10^{-6}$ cm^2·s^{-1}. Then it is calculated that the slope, k, of the fitting line for ln$D$ *vs* $1/T$ in Figure 3 is equal to −300.7. On the other hand, the diffusion coefficient, D, in accordance with the Arrhenius function is:

$$D = D_0 \cdot e^{-Q/RT}, \quad [3]$$

where D_0 is the constant diffusion coefficient; Q is the diffusion activation energy; T is temperature in K and R is the gas constant 8.314 J·mol^{-1}·K^{-1}. The natural logarithm of Eq. [3] is:

$$\ln D = \ln D_0 - \frac{Q}{RT}. \quad [4]$$

Therefore, the fitting line slope, k, is:

$$k = -\frac{Q}{R}. \quad [5]$$

The diffusion activation energy, Q, is:

$$Q = -kR. \quad [6]$$

Substituting the values of k and R into Eq. [6] yields the nitrogen diffusion activation energy in hexagonal nuclear graphite, $Q \approx 2.5$ kJ·mol^{-1}.

B. *Two- and Three-Dimensional Pore Morphology and Porosity*

The total porosity of nuclear graphite, A, was calculated using the Archimede's weight-volume method, given by:

$$A = \frac{\rho_{\text{True}} - \rho_{\text{Apparent}}}{\rho_{\text{True}}} \times 100 \text{ pct}, \quad [7]$$

where ρ_{True} is the true density, 2.123 g·cm^{-3} for the graphite specimens measured by mercury porosimetry; ρ_{Apparent} is the apparent density equal to the ratio of the mass, m, and the apparent volume, V_{Apparen}. In the tests, the mass of each graphite specimen was characterized by the ML204 electronic balance, and the apparent volume was calculated as $V_{\text{Apparent}} = 4/3\pi r^{3.}$ after accurate diameter measurement of the spherical specimens using micrometer three times. Figure 4 shows the total porosity for all nano- and micro-pores at different temperatures. The error bar of each value was calculated according to the variance of the small sample (≤30). It is found that the graphite porosity of roughly 20 pct was almost unchanged in the nitrogen diffusion processes, indicating constant combined volume of micro- and nano-pores. First, two-dimensional surface morphology of the 0.5 to 2 μm micro-pores, as shown in Figures 5(a) through (e), demonstrates that these pores were distributed randomly and the micro-pore area became larger as temperature increased. At 873 K (600 °C), there were fewer micro-pores than at 673 K and 1073 K (400 °C and 800 °C). In Figure 5(f), the area fraction of the 0.5 to 2 μm micro-pores increased from 0.14 pct at room temperature to 6.36 pct at 1073 K (800 °C), and the value at 873 K (600 °C) was less than at 673 K and 1073 K (400 °C and 800 °C). When these micro-pores were approximately small spheres, the porosity was proportional to the pore area fraction and presented a similar rising tendency with temperature. Second,

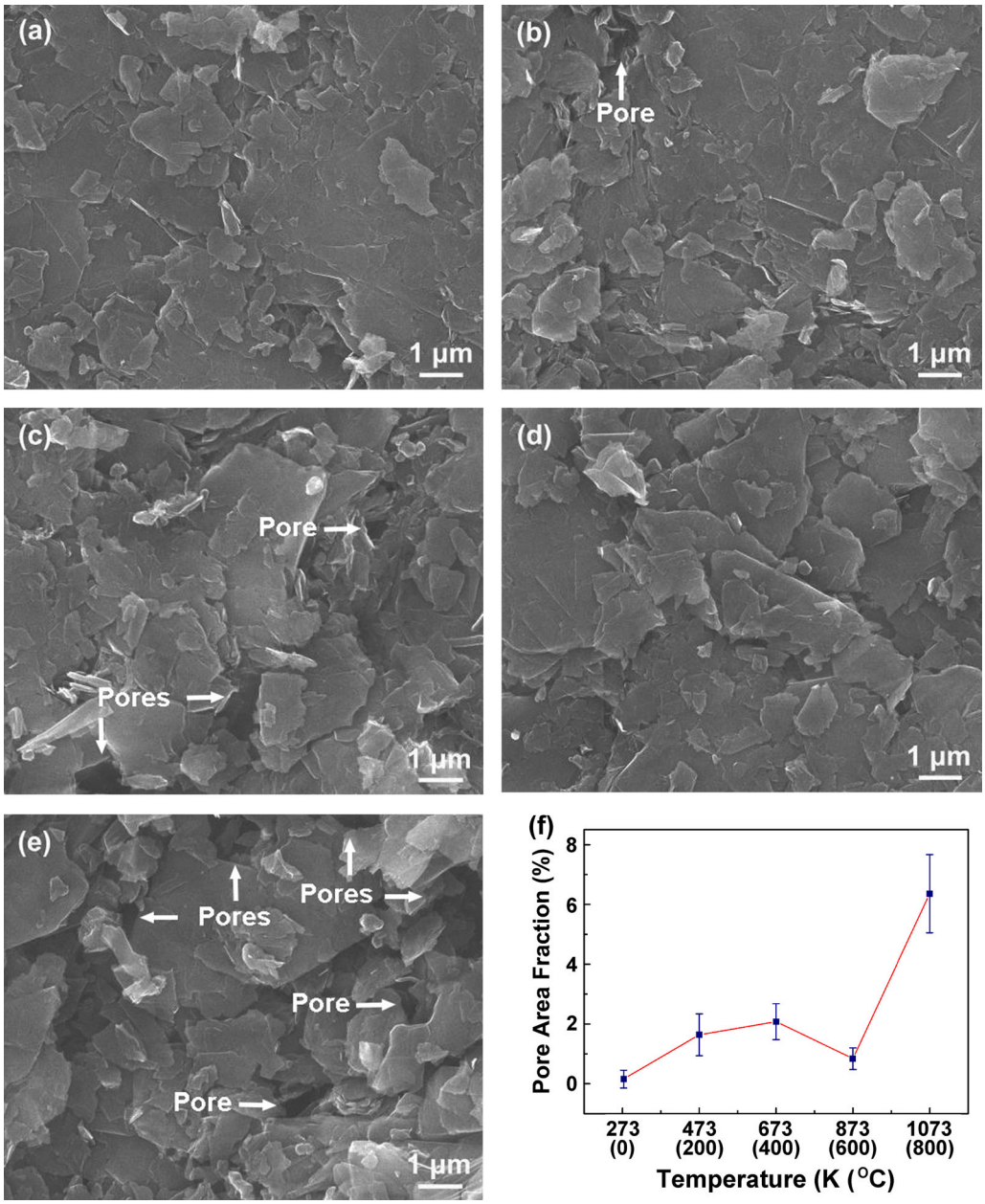

Fig. 5—Two-dimensional surface morphology and pore area fraction of graphite specimens after nitrogen diffusion at different temperatures: (*a*) Room temperature [approximately 293 K (20 °C)], (*b*) 473 K (200 °C), (*c*) 673 K (400 °C), (*d*) 873 K (600 °C), (*e*) 1073 K (800 °C), and (*f*) area fraction for the 0.5 to 2 μm micro-pores on the basis of the ratio of the pore area and the total figure area in Figs. 5(a) through (e).

three-dimensional construction of the micro-pores with the diameter >2 μm by XCT in Figure 6 manifests that the pores were obviously enlarged, and their aggregation and connection with each other occurred typically around the surface and the center of the specimen after nitrogen diffusion at 1073 K (800 °C). Quantitatively, relative porosity of the same specimen before and after high-temperature nitrogen diffusion was accurately calculated in accordance with the exterior-inside threshold value of the image gray scale of 55 in the 0 to 255 range. The relative central-zone porosity of the micro-pores in Figures 6(a) and (b) increased from 0.56 to 0.7 pct, while the relative porosity near the surface in Figures 6(c) and (d) ranged from 0.9 to 2.02 pct, as shown in Figure 6(e). It is illustrated that the variation of the relative porosity was larger at the near-surface zone than at the central zone. The average of the relative porosity for the >2 μm micro-pores at the central and near-surface zones increased to 1.36 pct after nitrogen diffusion, about twice as large as the relative porosity, 0.73 pct, before nitrogen diffusion. Third, the volume-diameter and porosity-temperature plots for the 2 to 500 nm nano-pores were measured using the BET method, as shown in Figure 7. Although the diameter of the nano-pores with the largest volume was about 1 to 2 nm at different temperatures, the decreasing tendency of the porosity

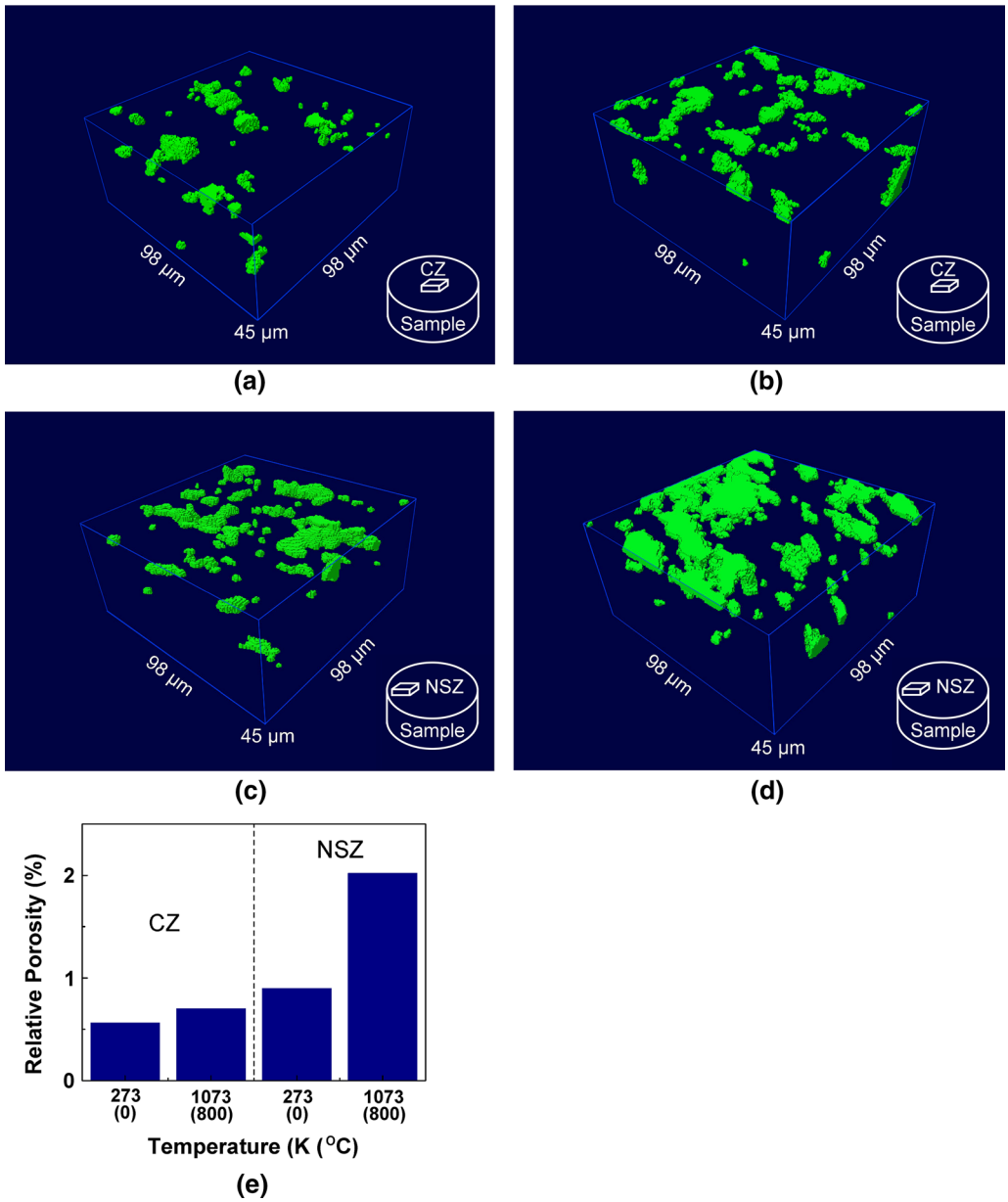

Fig. 6—Three-dimensional structures and distribution of >2 μm micro-pores by XCT in the central zones (CZ) (*a*) before and (*b*) after nitrogen diffusion at 1073 K (800 °C), and in near-surface zones (NSZ) (*c*) before and (*d*) after nitrogen diffusion at 1073 K (800 °C), respectively, and (*e*) relative porosity for the micro-pores in the central and near-surface zones before and after nitrogen diffusion at 1073 K (800 °C), where green color represents micro-pores. It is shown that the micro-pores became larger, while pore aggregation occurred after nitrogen diffusion at 1073 K (800 °C).

was presented when the temperature changed from room temperature to 1073 K (800 °C). For instance, the porosity at 1073 K (800 °C), 0.44 pct, was approximately half of 0.75 pct at 293 K (20 °C). Besides, the anomalous phenomenon also took place, and the maximum nano-pore volume was at 873 K (600 °C).

In short, the multi-scale results indicate that the volume of the 0.5 to 2 μm and >2 μm micro-pores in nuclear graphite were enlarged at higher temperatures, and for the nano-pores with the 2 to 500 nm diameter the inverse variation emerged. The porosity at 1073 K (800 °C) demonstrates that the porosity increment for the micro-pores was approximately equal to its reduction for the nano-pores. That is, the coalescence of the nano-pores into the micro-pores induced the increase of the micro-pore volume, the decrease of the nano-pore volume and the unchanged total porosity. At 873 K (600 °C), more nano-pores with smaller volume were formed.

C. *Multi-Scale Pore Evolution Mechanisms*

The remarkable effects of temperature on microscopic and nano-scale hexagonal structures of bulk graphite

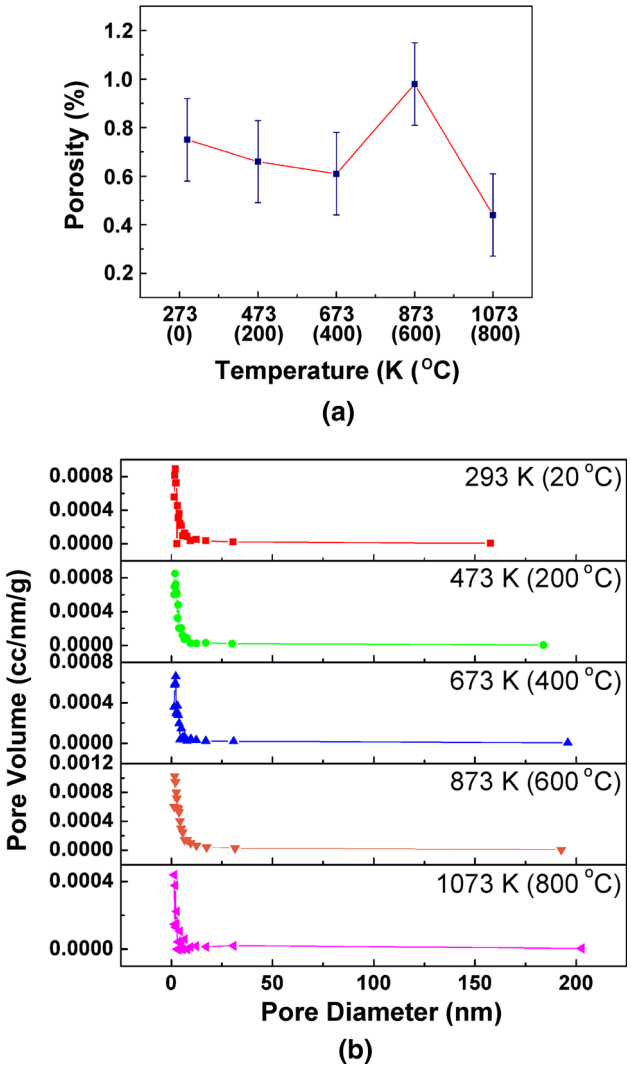

Fig. 7—(*a*) Porosity and (*b*) pore volume with the diameter of 2-500 nm nano-pores after nitrogen diffusion at different temperatures: Room temperature [approximately 293 K (20 °C)], 473 K, 673 K, 873 K, and 1073 K (200 °C, 400 °C, 600 °C and 800 °C).

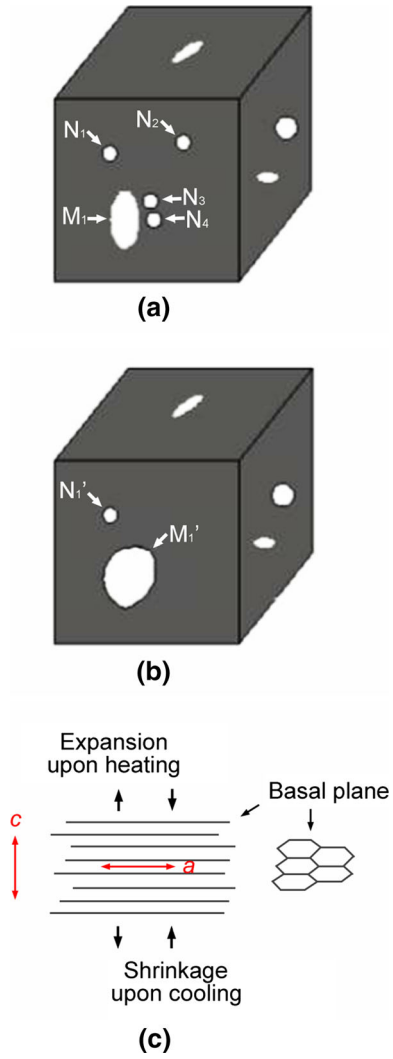

Fig. 8—Schematics of temperature-dependent multi-scale nuclear graphite pore evolution mechanisms: (*a*) virgin morphology of nano-pores "N_1 - N_4" and a micro-pore "M_1," (*b*) morphology of a nano-pore "N_1'" and a fresh micro-pore "M_1'" after nitrogen diffusion at high temperatures, and (*c*) lattice expansion or shrinkage in *a* and *c* directions upon heating or cooling, where the nano-pores such as "N_2" were capable of being closed in the heating processes, and the coalescence of the pores "M_1," "N_3," and "N_4" along with the formation of the fresh micro-pore "M_1'" occurred upon cooling.

have been detected, such as heterogeneous thermal expansion and cooling shrinkage at high-temperature vacuum, collapse of basal plane vacancies, and ballistic displacement of carbon atoms in neutron-irradiation conditions at different temperatures.[18,28,38–40] In this work, it is found that the volume of the >0.5 μm diameter micro-pores consisting of open and closed pores was enlarged, yet there were fewer nano-pores with 2-500 nm diameter at higher temperature. The porosity increment for the micro-pores was approximately equal to its reduction for the nano-pores at 1073 K (800 °C). For the bulk graphite, localized deformation, including initiation and propagation of the Mrozowski cracks as well as the closure of the defects, could take place owing to significantly inhomogeneous thermal expansion and cooling shrinkage in *a* and *c* directions.[28,41–43] For instance, the nano-pore "N_2" shown in Figure 8 was capable of closing upon heating,[28] inducing the reduction of the nano-pore volume at higher temperature. On the other hand, the nitrogen-diffused graphite specimens at high temperature were immediately cooled by the room temperature helium in the fourth experimental stage. The localized lattice shrinkage with the CTE of 20 to 40 $\times$ 10^{-6} K^{-1} in the *c* direction and 1.5 $\times$ 10^{-6} K^{-1} in the *a* direction occurred in the graphite specimens during the cooling processes, and the Mrozowski cracks on basal planes possibly nucleated due to internal stress relief.[41–43] As shown in Figure 8, larger pores, such as the micro-pore "M_1'," could be formed if the cracks nucleated and grew in ligaments between the sub-scale neighboring pores "M_1," "N_3," and "N_4," and the pores coalesced with each other. Moreover, collapse of vacancies on basal planes and ballistic displacement of carbon atoms probably occurred at high temperatures.

In addition, mild oxidation of nuclear graphite might take place, since the gases consisted of ≤3 ppm O_2, ≤1 ppm H_2, ≤3 ppm ΣC (CO and CO_2), and ≤6 ppm H_2O apart from nitrogen in the TGA experiments. Oxidation mechanisms were different at various temperatures.[7,9–15] Open pores were first oxidized below 873 K (600 °C), and the oxidation rate became slower in open pores due to the restricted oxygen diffusion rate at temperatures ranging from 873 K to 1123 K (600 °C to 850 °C). Then oxidation reactions ceased in open pores, and just the external graphite surfaces were oxidized above approximately 1123 K (850 °C). From this perspective, localized active surfaces of the open pores including nano- and micro-pores promoted the formation of the larger pores at 673 K (400 °C), inducing the decrease of the nano-pore volume and the porosity increase for the micro-pores. At 873 K (600 °C), the oxidation rate was small within the open pores and on the external specimen surfaces. As a consequence, the nano- and micro-pore size became a little larger, which made fewer nano-pores transformed to the micro-pores at 873 K (600 °C) than at 673 K (400 °C). The larger nano-pore volume and the smaller micro-pore volume were also formed at 873 K (600 °C) than at 673 K (400 °C). At 1073 K (800 °C), the oxidation reactions almost ceased inside the open pores and mainly occurred on the external specimen surfaces, in favor of the formation of the larger micro-pore volume at the near-surface zone than at the central zone.

As mentioned above, the localized oxidation might play some role in the multi-scale pore evolution behavior at 673 K, 873 K and 1073 K (400 °C, 600 °C and 800 °C), but the primary factor for controlling graphite microstructure evolution at temperatures ranging from 293 K to 1073 K (20 °C to 800 °C) should be temperature owing to the extremely low oxidative gas content. This is also justified by the almost unchanged total porosity at different temperatures in Figure 4, and approximately equal reduction and increment of the porosity separately for the nano- and micro-pores at 1073 K (800 °C) in Figures 6(e) and 7(a), along with the occurrence of the multi-pore evolution without oxidation at 473 K (200 °C) in Figures 5(f) and 7(a).

IV. CONCLUSIONS

(1) Stable weight loss of nuclear graphite during nitrogen diffusion processes gradually increased with temperature, which was mainly associated with the nitrogen molecules escaping from the graphite matrix to outside. Nitrogen diffusion activation energy was approximately 2.5 $kJ \cdot mol^{-1}$. Since the peak value of stable weight loss first emerged at 573 K to 673 K (300 °C to 400 °C), porous nuclear graphite, before being placed into HTGRs, should be subjected to vacuum at 573 K to 673 K (300 °C to 400 °C) in order to minimize ^{14}N in the pores and ^{14}C generated during HTGRs operation.

(2) The volume of the nano-pores with 2 to 500 nm diameter decreased with temperature, possibly owing to the lattice expansion upon heating. Larger porosity for the micro-pores with 0.5 to 2 μm and >2 μm diameters at higher temperature should be mainly induced by fracture of the ligaments between the neighboring pores and the coalescence of the sub-scale pores during the cooling process. Besides, localized oxidation of nuclear graphite might play some role on the multi-scale pore evolution behavior at 673 K, 873 K and 1073 K (400 °C, 600 °C and 800 °C).

ACKNOWLEDGMENTS

The authors would like to thank Dr. Yanan Fu, Dr. Biao Deng, and Dr. Rongchang Chen at the Shanghai Synchrotron Radiation Facility for help with X-ray imaging. The authors also acknowledge funding provided by the project from China Postdoctoral Science Foundation under the Grant 2016M591164 and the National Science and Technology Major Projects under the grant ZX06901.

REFERENCES

1. X.W. Zhou, Z.L. Yi, Z.M. Lu, J. Zhang, and S.Y. Yu: *Carbon Technol.*, 2012, vol. 31, pp. B9–B13.
2. Z. Hu, Z.C. Li, Z. Zhou, C.Q. Shi, H. Schut, and K. Pappas: *J. Phys: Conf. Ser.*, 2014, vol. 505, p. 012104.
3. D.Y. Chen, Z.C. Li, W. Miao, and Z.J. Zhang: *Mater. Trans.*, 2012, vol. 53, pp. 159–63.
4. Z. Hu, Z.C. Li, D.Y. Chen, W. Miao, and Z.J. Zhang: *J. Nucl. Sci. Technol.*, 2014, vol. 51, pp. 487–92.
5. T. Lowe, R.S. Bradley, S. Yue, K. Barii, J. Gelb, N. Rohbeck, J. Turner, and P.J. Wither: *J. Nucl. Mater.*, 2015, vol. 461, pp. 29–36.
6. J. Kane, C. Karthik, D.P. Butt, W.E. Windes, and R. Ubic: *J. Nucl. Mater.*, 2011, vol. 415, pp. 189–97.
7. D. Vulpius, K. Baginski, C. Fischer, and B. Thomauske: *J. Nucl. Mater.*, 2013, vol. 438, pp. 163–77.
8. W.H. Huang, S.C. Tsai, C.W. Yang, and J.J. Kai: *J. Nucl. Mater.*, 2014, vol. 454, pp. 149–58.
9. W.H. Huang, S.C. Tsai, I.C. Chiu, C.H. Chen, and J.J. Kai: *Nucl. Eng. Des.*, 2014, vol. 271, pp. 270–74.
10. L. Babout, P.M. Mummery, T.J. Marrow, A. Tzelepi, and P.J. Withers: *Carbon*, 2005, vol. 43, pp. 765–74.
11. M.S. EI-Genk and J.M. Tournier: *Carbon*, 2005, vol. 43, pp. 765–74.
12. L. Babout, T.J. Marrow, P.M. Mummery, and P.J. Withers: *Scripta Mater.*, 2006, vol. 54, pp. 829–34.
13. L. Babout, B.J. Marsden, P.M. Mummery, and T.J. Marrow: *Acta Mater.*, 2008, vol. 56, pp. 4242–54.
14. C. Berre, S.L. Fok, P.M. Mummery, J. Ali, B.J. Marsden, T.J. Marrow, and G.B. Neighbour: *J. Nucl. Mater.*, 2008, vol. 381, pp. 1–8.
15. L.R. Radovic, A.B. Silva-Tapia, and F. Vallejos-Burgos: *Carbon*, 2011, vol. 49, pp. 4218–25.
16. P. Wang, C.I. Contescu, S.Y. Yu, and T.D. Burchell: *J. Nucl. Mater.*, 2012, vol. 430, pp. 229–38.
17. B.T. Kelly: *Carbon*, 1982, vol. 20, pp. 1–3.
18. J.E. Brocklehurst and B.T. Kelly: *Carbon*, 1993, vol. 31, pp. 179–83.
19. D.K.L. Tsang, B.J. Marsden, S.L. Fok, and G. Hall: *Carbon*, 2005, vol. 43, pp. 2902–06.
20. T. Trevethan and M.I. Heggie: *Comput. Mater. Sci.*, 2016, vol. 113, pp. 60–65.
21. C.K. Chang, S.C. Tsai, J.J. Kai, C.P. Chuang, and E.W. Huang: *Proc. Eng.*, 2012, vol. 36, pp. 7–12.

22. S.C. Tsai, E.W. Huang, J.J. Kai, and F.R. Chen: *J. Nucl. Mater.*, 2013, vol. 434, pp. 17–23.
23. A.A. Campbell and G.S. Was: *Carbon*, 2014, vol. 77, pp. 993–1010.
24. A.A. Campbell, Y. Katoh, M.A. Snead, and K. Takizawa: *Carbon*, 2016, vol. 109, pp. 860–73.
25. A.A. Campbell, K.B. Campbell, and G.S. Was: *Carbon*, 2013, vol. 60, pp. 410–20.
26. R. Krishna, A.N. Jones, L. McDermott, and B.J. Marsden: *J. Nucl. Mater.*, 2015, vol. 467, pp. 557–65.
27. C. Karthik, J. Kane, D.P. Butt, and W.E. Windes: *Carbon*, 2015, vol. 86, pp. 124–31.
28. K.Y. Wen, J. Marrow, and B. Marsden: *J. Nucl. Mater.*, 2008, vol. 381, pp. 199–203.
29. T.J. Marrow, D. Liu, S.M. Barhli, L. Saucedo Mora, Y. Vertyagina, D.M. Collins, C. Reinhard, S. Kabra, P.E.J. Flewitt, and D.J. Smith: *Carbon*, 2016, vol. 96, pp. 285–302.
30. M. Mostafavi, S.A. McDonald, H. Cetinel, P.M. Mummery, and T.J. Marrow: *Carbon*, 2013, vol. 59, pp. 325–36.
31. M. Mostafavi, N. Baimpas, E. Tarleton, R.C. Atwood, S.A. McDonald, A.M. Korsunsky, and T.J. Marrow: *Acta Mater.*, 2013, vol. 61, pp. 6276–89.
32. M. Mostafavi, S.A. McDonald, P.M. Mummery, and T.J. Marrow: *Eng. Fract. Mech.*, 2013, vol. 110, pp. 410–20.
33. M. Mostafavi, M.J.J. Schmidt, B.J. Marsden, and T.J. Marrow: *Mater. Sci. Eng. A*, 2012, vol. 558, pp. 265–77.
34. A. King, G. Johnson, D. Engelberg, W. Ludwig, and J. Marrow: *Science*, 2008, vol. 321, pp. 382–85.
35. L.K. Zhu, Y. Yan, J.X. Li, L.J. Qiao, and A.A. Volinsky: *Corros. Sci.*, 2014, vol. 80, pp. 350–58.
36. M. Uhmemann and B.G. Pound: *Corros. Sci.*, 1998, vol. 40, pp. 645–62.
37. G. Wang, Y. Yan, J.X. Li, J.Y. Huang, Y.J. Su, and L.J. Qiao: *Corros. Sci.*, 2013, vol. 77, pp. 273–80.
38. C. Karthik, J. Kane, D.P. Butt, W.E. Windes, and R. Ubic: *Microsc. Microanal.*, 2012, vol. 18, pp. 272–78.
39. M. Heerschap and E. Schuller: *Carbon*, 1969, vol. 7, pp. 624–25.
40. P.A. Thrower and W.N. Reynolds: *J. Nucl. Mater.*, 1963, vol. 8, pp. 221–26.
41. S. Mrozowski: *Proc. Conf. Carbon*, 1954, vol. 31, pp. 31–45.
42. A.L. Sutton and V.C. Howard: *J. Nucl. Mater.*, 1962, vol. 1, pp. 58–71.
43. H.M. Freeman, A.N. Jones, M.B. Ward, F.S. Hage, N. Tzelepi, Q.M. Ramasse, A.J. Scott, and R.M.D. Brydson: *Carbon*, 2016, vol. 103, pp. 45–55.